2018

Direct observation of a two-dimensional hole gas at oxide interfaces

H. Lee, N. Campbell, J. Lee, T. Asel, T. Paudel, H. Zhou, J. W. Lee, B. Noesges, J. Seo, B. Park, L. J. Brillson, S. H. Oh, E. Y. Tsymbal, M. S. Rzchowski, and C. B. Eom

Direct observation of a two-dimensional hole gas at oxide interfaces

H. Lee[1], N. Campbell[2], J. Lee[3], T. J. Asel[4], T. R. Paudel[5], H. Zhou[6], J. W. Lee[1], B. Noesges[4], J. Seo[3], B. Park [ID][3,7], L. J. Brillson[4,8], S. H. Oh[3], E. Y. Tsymbal[5], M. S. Rzchowski[2] and C. B. Eom[1]*

The discovery of a two-dimensional electron gas (2DEG) at the LaAlO₃/SrTiO₃ interface[1] has resulted in the observation of many properties[2–5] not present in conventional semiconductor heterostructures, and so become a focal point for device applications[6–8]. Its counterpart, the two-dimensional hole gas (2DHG), is expected to complement the 2DEG. However, although the 2DEG has been widely observed[9], the 2DHG has proved elusive. Herein we demonstrate a highly mobile 2DHG in epitaxially grown SrTiO₃/LaAlO₃/SrTiO₃ heterostructures. Using electrical transport measurements and in-line electron holography, we provide direct evidence of a 2DHG that coexists with a 2DEG at complementary heterointerfaces in the same structure. First-principles calculations, coherent Bragg rod analysis and depth-resolved cathodoluminescence spectroscopy consistently support our finding that to eliminate ionic point defects is key to realizing a 2DHG. The coexistence of a 2DEG and a 2DHG in a single oxide heterostructure provides a platform for the exciting physics of confined electron–hole systems and for developing applications.

Since the discovery of quasi-two-dimensional (2D) electron conduction at an interface between insulating oxide layers[1], various oxide heterointerfaces have been intensively studied to understand the underlying physics and appreciate the origin of the intriguing interfacial conduction[10–14]. The emergence of the 2D-confined electrons at oxide heterointerfaces is often explained by the 'polar catastrophe' mechanism[10]. In this model, when a positively charged atomic layer of one material forms an interface with a charge-neutral atomic layer of the other material, an electric field that points away from the interface to the top surface is generated because of the polarity discontinuity. The resulting electrostatic potential diverges as the thickness of the heterostructure grows. To avoid such potential divergence, negative-charge carriers accumulate at the interface to create a so-called n-type interface. Similarly, a p-type interface can be envisaged at the interface between a negatively charged and a charge-neutral atomic layer. As the 2DEG at n-type interfaces exhibits remarkable physical properties[2–5], p-type interfaces, where 2DHG is expected to form, have also attracted considerable interest. However, during the almost 15 years since the discovery of 2DEG at an n-type interface, a direct observation of 2DHG has not been reported to date. Even though the theoretical studies have predicted 2D-confined hole carriers at such interfaces[15,16], most of the experimentally tested p-type interfaces exhibited an insulating behaviour[1,10]. Evidence for the occurrence of electron–hole bilayer in oxides was provided by magnetotransport studies, ultraviolet photoelectron spectroscopy[17] and scanning tunnelling microscopy[18]. However, a p-type conduction with exclusively holes as carriers has not yet been demonstrated. The lack of a clear explanation for such asymmetric behaviour of the p- and n-type interfaces makes this topic more intriguing.

A p-type interface can be built by growing a non-polar oxide thin film on the negatively charged substrate surface. Here, we chose (001) SrTiO₃/LaAlO₃/SrTiO₃ (STO/LAO/STO) heterostructures to realize the 2DHG. As shown in Fig. 1a, if the STO substrate is TiO₂-terminated, p-type and n-type interfaces are expected to form at the top and bottom of the STO/LAO/STO heterostructure, respectively, to avoid a polar catastrophe. Indeed, our first-principles calculations (Supplementary Fig. 1) demonstrate the accumulation of electrons at the bottom n-type interface and holes at the top p-type interface. The polar discontinuity may, however, also be resolved by the accumulation of positively charged oxygen vacancies at the top interface[10,19]. This is evident from our first-principles calculations, which indicate the absence of 2DHG when oxygen vacancies are formed in STO or LAO close to the top interface. This implies that, even though one can fabricate a high-quality p-type interface, the interface may still be electrically insulating because of the ionized oxygen vacancies. Therefore, to realize 2DHG practically, we focus on two issues: (1) to build an atomically-sharp p-type interface that consists of SrO/AlO₂ layers and (2) to minimize oxygen vacancies near the p-type interface.

We synthesized STO/LAO thin films by pulsed-laser deposition (PLD) with in situ monitoring of reflection high-energy electron diffraction (RHEED) on TiO₂-terminated (001) STO substrates (Supplementary Fig. 2). To minimize the oxygen-vacancy formation during the growth, oxygen partial pressure in the chamber was kept as high as 10^{-3} mbar for LAO growth and 10^{-2} mbar for STO growth, respectively. Typical samples described in the literature are grown at oxygen partial pressures lower than 10^{-4} mbar[1,10]. The samples were also in situ post-annealed in the oxygen ambient. Scanning transmission electron microscopy–annular dark-field (STEM–ADF) images taken from the STO/LAO/STO heterostructure are given in Fig. 1b. The top STO/LAO interface is atomically abrupt and smooth (Supplementary Fig. 3). Such an atomically well-defined interface is essential to realize 2DHG because the atomic intermixing at the interface can reduce the potential difference in between the consecutive layers and negate the interface-band bending that is crucial for

[1]Department of Materials Science and Engineering, University of Wisconsin-Madison, Madison, WI, USA. [2]Department of Physics, University of Wisconsin-Madison, Madison, WI, USA. [3]Department of Energy Science, Sungkyunkwan University (SKKU), Suwon, Korea. [4]Department of Physics, The Ohio State University, Columbus, OH, USA. [5]Department of Physics and Astronomy, Nebraska Center for Materials and Nanoscience, University of Nebraska, Lincoln, NE, USA. [6]X-Ray Science Division, Advanced Photon Source, Argonne National Laboratory, Argonne, IL, USA. [7]Department of Materials Science and Engineering, Pohang University of Science and Technology (POSTECH), Pohang, Korea. [8]Department of Electrical and Computer Engineering, The Ohio State University, Columbus, OH, USA. *e-mail: eom@engr.wisc.edu
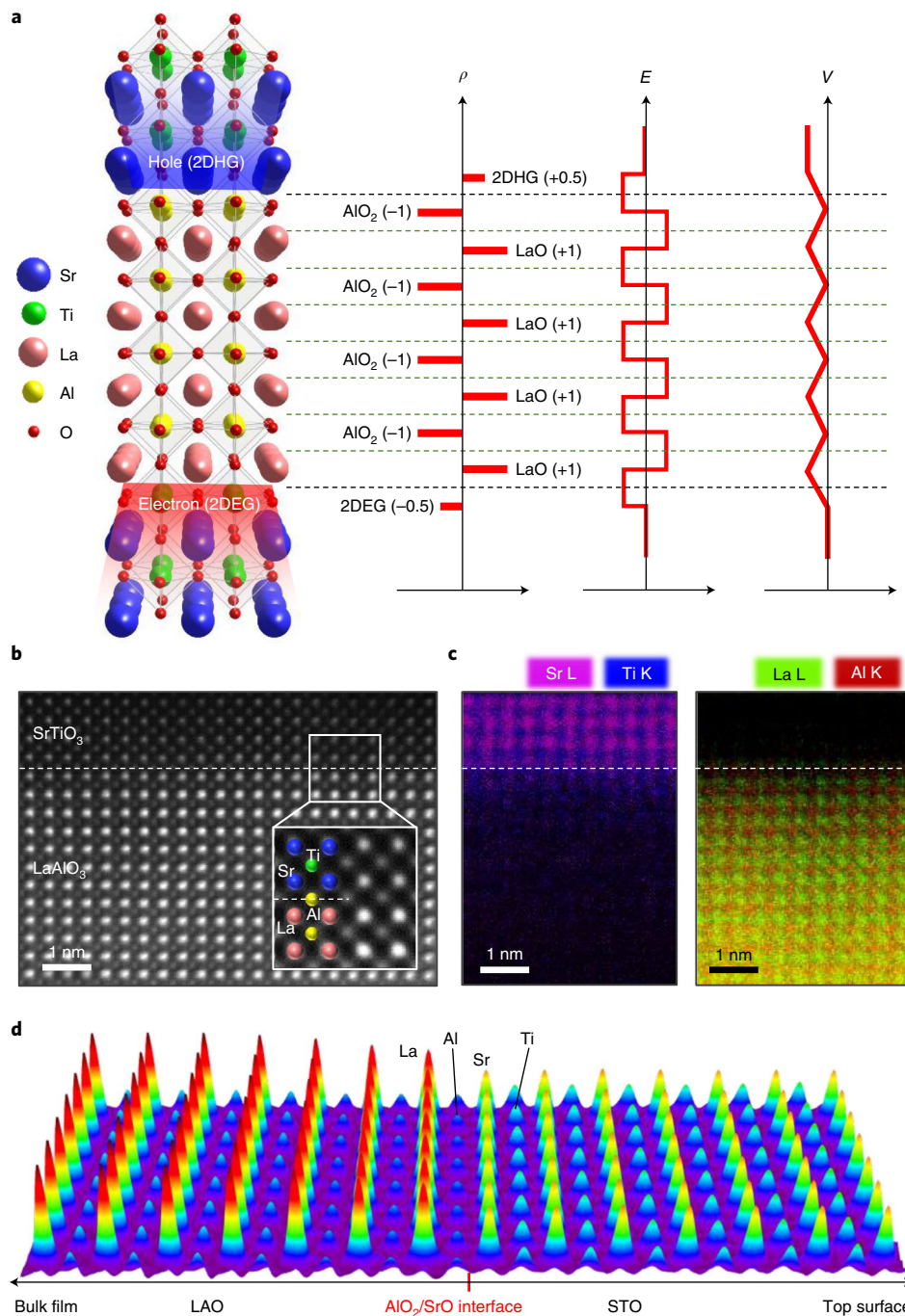
Fig. 1 | Atomically abrupt p-type interface in epitaxially grown STO/LAO/STO heterostructure. a, Schematics that depict the electronic reconstruction across the oxide heterostructure. The polar catastrophe mechanism suggests that the non-zero electric field from the polarity discontinuity at the heterointerfaces needs to be compensated to avoid potential divergence. At the bottom interface of $(LaO)^+/(TiO_2)^0$, the polar instability is resolved by 2D-confined electrons (shaded red). At the top interface of $(SrO)^0/(AlO_2)^-$, hole carriers can resolve the polar instability (shaded blue). **b**, STEM–ADF images obtained at the top interface. The inset shows the filtered image with a higher magnification and the atomic configuration (coloured). **c**, EDS elemental mapping of the same sample. The interface is atomically abrupt, and intermixing is not significant. **d**, COBRA-derived cation electron-density map across the top STO/LAO interface. The interface is atomically abrupt and consists of SrO and AlO_2 layers, as we designed.

the interfacial charge confinement. The magnified atomic structure (Fig. 1b inset) indicates that a high-quality SrO/AlO_2 interface has been built between the top STO and LAO thin films. Atomic-scale energy-dispersive X-ray spectroscopy (EDS) elemental mapping was performed on the same sample (Fig. 1c). The EDS maps show the chemically abrupt top interface with atomic intermixing limited to about a one unit cell.

To verify the atomic structure in more detail, synchrotron X-ray crystal truncation rod (CTR) measurements were performed, and analysed by the coherent Bragg rod analysis (COBRA) method (Supplementary Fig. 4). Fig. 1d shows the COBRA-derived cation electron-density map across the top interface. The electron density sharply changes at the interfaces, which indicates the high quality of the interface with minimal intermixing. The clearly
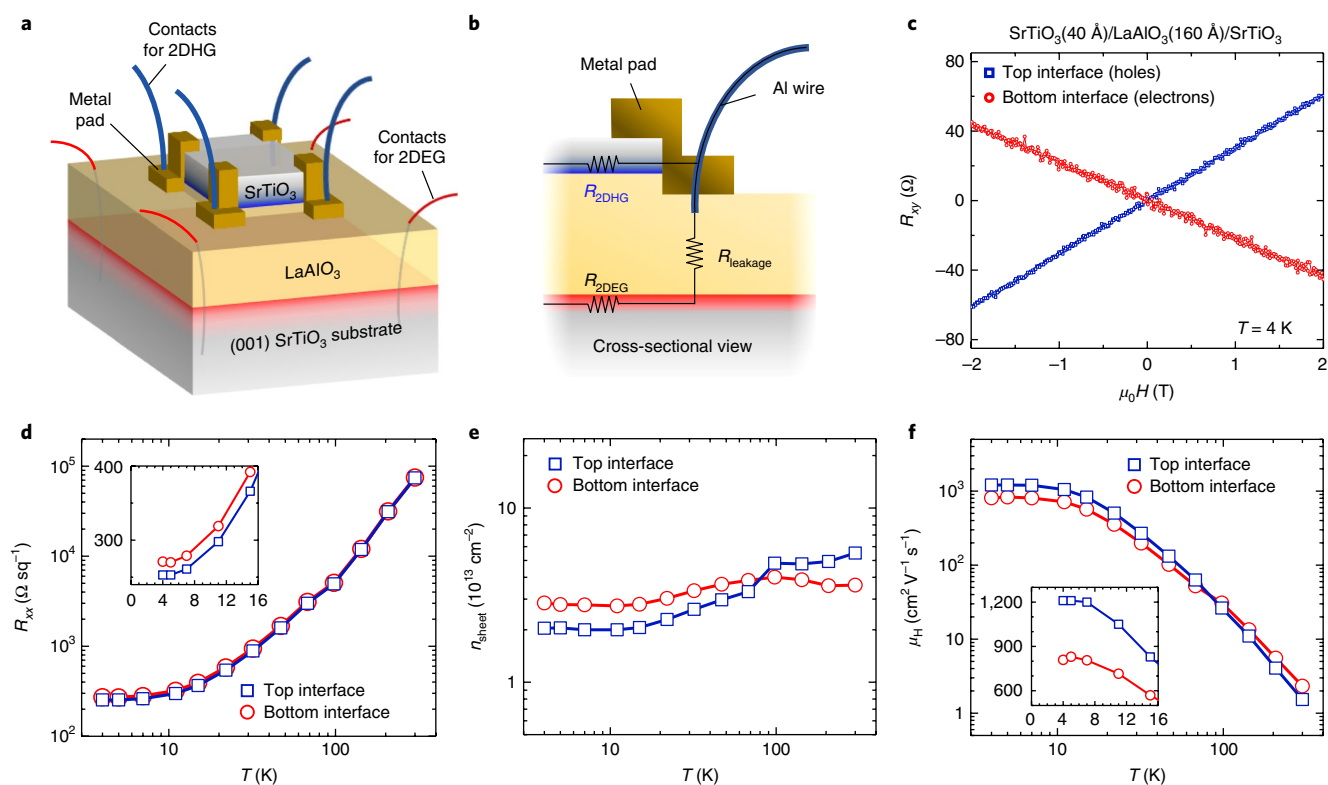
Fig. 2 | Electrical transport properties of the top and bottom interfaces in the STO/LAO/STO heterostructure. a, Schematic that depicts the electrical contact structures for the top and bottom interfaces. **b**, Cross-sectional view of the electrical contacts for the top interface. **c**, Hall resistance R_{xy} versus magnetic field $\mu_0 H$ for the top and bottom interfaces at 4 K. The top interface clearly shows a positive slope, which indicates p-type conductivity, whereas the bottom interface shows a negative slope, which indicates n-type conductivity. **d**, Temperature dependency of sheet resistance $R_{xx}(T)$ for the top (blue squares) and the bottom (red circles) interfaces. The inset shows R_{xx} values at a low temperature in linear scale. **e**, Temperature dependency of sheet carrier density $n_{sheet}(T)$ for the interfaces. **f**, Temperature dependency of mobility $\mu_H(T)$ for the interfaces. The inset shows the μ_H values at a low temperature in linear scale.

discernible difference in integrated electron numbers at the inter-face (Supplementary Fig. 4e) shows that the top interface consists of SrO and AlO$_2$ layers as we designed. This consistency between our atomic design and the actual atomic structure is important because non-uniform atomic terminations or severe atomic intermixing at the interface involve intricate and non-trivial phenomena that affect the overall band structures in oxide heterostructures[10,20] and may be detrimental to the 2DHG formation.

We examined the electrical transport properties of the top and bottom interfaces in the STO/LAO/STO heterostructure. To mea-sure the transport of each interface, the top STO film is square patterned and four corners of the STO are covered by metal pads (Supplementary Fig. 5). In this way, the top interface can be con-tacted by the metal pads, whereas the bottom interface can be con-tacted along the outer edge by conventional wire bonding (Fig. 2a). The magnetic-field-dependent Hall resistance $R_{xy}(H)$ is given in Fig. 2c. The top interface clearly shows a positive Hall coefficient, whereas the bottom interface shows a negative one. This indi-cates a hole-dominated conduction through the top interface and an electron-dominated conduction through the bottom interface. For comparison, we prepared an oxygen-deficient STO/LAO/STO heterostructure, but its top interface was completely insulating (Supplementary Fig. 6). Owing to the LAO layer being thin, a non-negligible leakage current exists between the top and bottom inter-faces (Fig. 2b). We modulated the leakage current by varying the contact structure, and observed that the Hall coefficient at the metal pads changed from positive to negative when the leakage current increased (Supplementary Fig. 7). Therefore, we conclude that the

positive Hall coefficient measured at the metal pads is determined by 2DHG rather than the leakage current. In the following analysis, we assume hole conduction for the top interface and electron con-duction for the bottom interface without considering the leakage effect. The relationship between the thickness of the films and the formation of 2DHG is investigated (Supplementary Figs. 8 and 9). When the top STO film was thicker than three unit cells, the sam-ples exhibited p-type conduction. As for the LAO, all the samples thinner than 120 unit cells showed p-type conduction.

The temperature-dependent sheet resistance, $R_{xx}(T)$, of the top and bottom interfaces are given in Fig. 2d. The R_{xx} of the interfaces were found to be similar to each other for a wide range of tempera-ture (4–300 K). The sheet carrier densities $n_{sheet}(T)$ of both interfaces are not strongly dependent on temperature (Fig. 2e). On the other hand, their Hall mobilities $\mu_H(T)$ showed a clear temperature depen-dence (Fig. 2f), consistent with that of previously reported 2DEG[1]. At low temperatures, the mobilities of both electrons and holes are nearly independent of temperature because the transport is domi-nated by defect scattering. At higher temperatures, the mobility decreases as phonon scattering comes to dominate the scattering.

That the mobility of 2DHG is comparable and even slightly higher than the mobility of 2DEG at low temperature (Fig. 2f inset) was not expected from the band structure, as holes have a higher effective mass than electrons. The calculated electron mass at the conduction band minimum is about $0.4m_o$ (Supplementary Fig. 10), where m_o represents the free electron mass. These val-ues are smaller than the effective hole mass of $1.2m_o$ calculated at the valence-band maximum. These estimates, however, do not
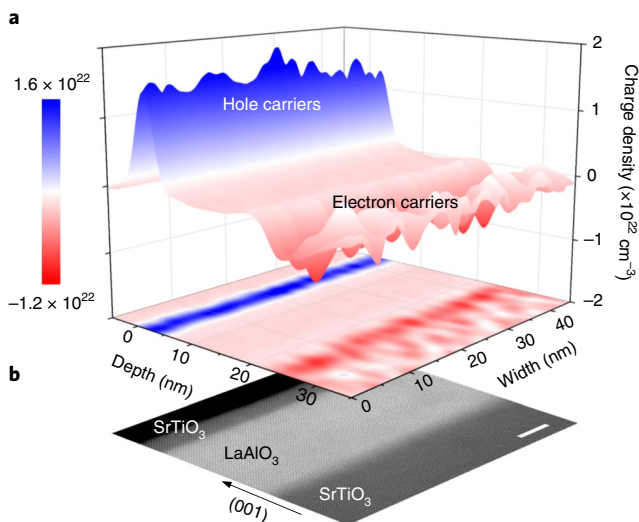
Fig. 3 | Charge distribution in the STO/LAO/STO heterostructure. a, The charge-density map of the STO/LAO/STO heterostructure obtained by the in-line electron holography technique. The top and bottom interfaces clearly show the positive and negative charges, respectively. **b**, The STEM–ADF image of the entire STO/LAO/STO heterostructure. Scale bar, 5 nm.

polarons[21]. As a result, the effective electron mass renormalizes to a larger value of $2.5m_o$. On the contrary, holes are weakly coupled to phonons, which is evident from the calculated electron–phonon coupling matrix element for the valence-band maximum being seven times smaller than that at the conduction-band minimum[22]. Hence, given the electron–phonon coupling, it is likely that the effective mass of the holes is comparable to or even smaller than the effective mass of electrons. This qualitatively explains the relatively large hole mobility being comparable to the electron mobility. The temperature dependence is largely controlled by the phonon-mode population[23], which results in the qualitatively similar behaviour of electron and hole mobilities (Fig. 2f) and resistivities (Fig. 2d) as a function of temperature. However, given the complementary interaction of the closely spaced top and bottom interfaces as well as the leakage-current effect, we expect that further studies are required to elucidate quantitatively the electrical properties of the completely isolated 2DHG.

Using in-line electron holography, we directly demonstrate that the 2DHG is, indeed, formed at the STO/LAO interface. The in-line electron holography, using a field-emission transmission electron microscope (FE-TEM), can map the internal charge distribution of oxide heterostructures by retrieving phase-shift information of the transmitted electron beam[24]. The charge-density map of the STO/LAO/STO heterostructure is given in Fig. 3a. The corresponding atomic structure is shown by a STEM image (Fig. 3b). A high density of positive charges is clearly observed at the top interface, whereas the bottom interface showed negative charges. Given the high conductivity at both interfaces, those positive and negative charges at each interface are apparently hole and electron carriers rather than
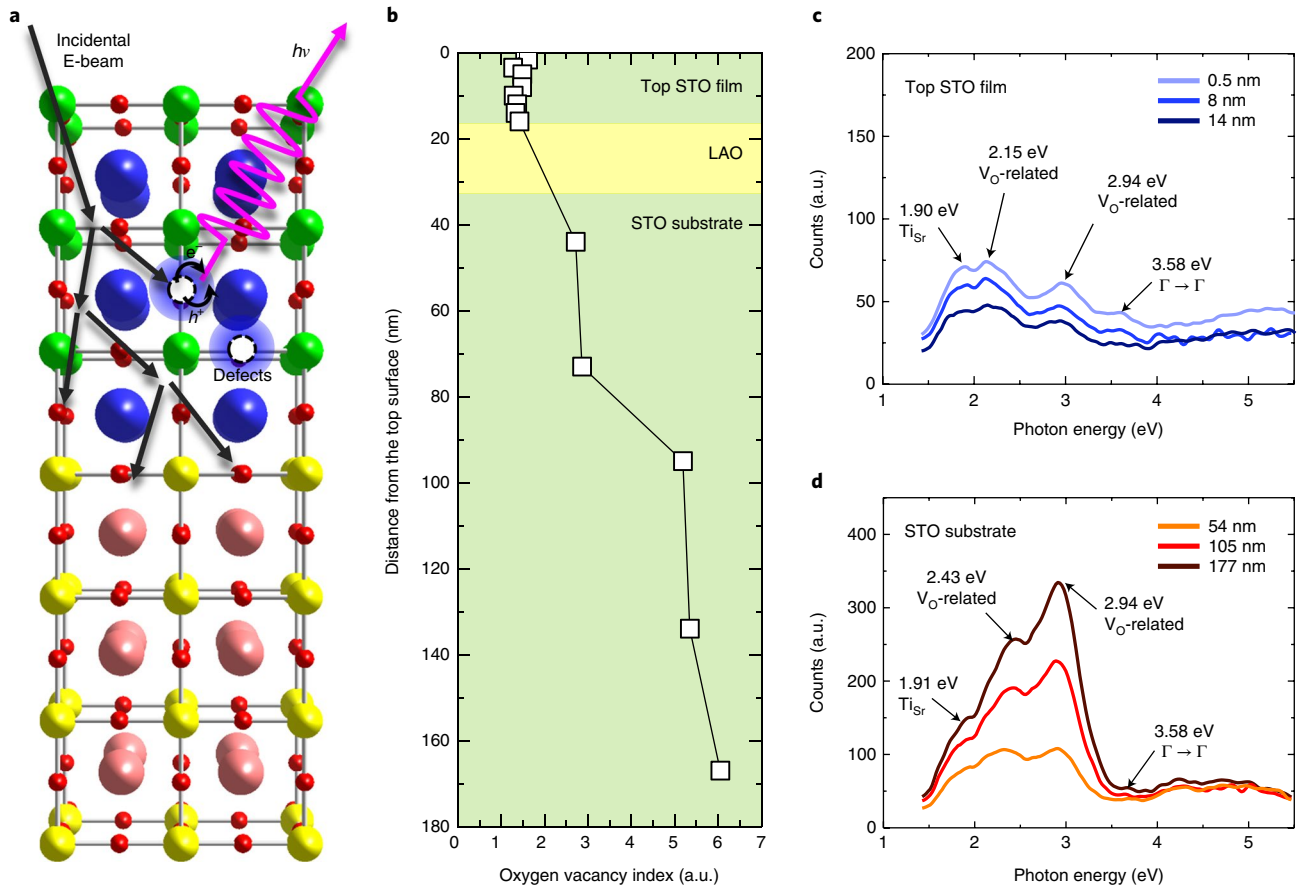
consider the electron–phonon coupling, which renormalizes the effective masses of carriers. The electrons are known to be strongly coupled to phonons in the LAO/STO system and form large

Fig. 4 | Oxygen-vacancy distribution in the STO/LAO/STO heterostructure. a, Schematic that depicts the mechanism of DR-CLS. By optically detecting the luminescence signals, the band-to-defect transitions can be detected as well as a band-to-band transition. **b**, Profile of the oxygen-vacancy index across the interfaces. **c,d**, The representative CLS data in the top STO film (**c**) and in the bulk STO substrate (**d**), respectively. V_O represents the oxygen vacancy.

localized ionic charges. If the large number of positive charges had originated mainly from ionized oxygen vacancies, this would have been seen as a local variation of the lattice spacing. However, the lattice-spacing profile obtained by 3D-COBRA (Supplementary Fig. 4f) does not show such signals.

The presence of holes at the top interface can be supported more strongly by verifying the lack of oxygen vacancies near the interface. An electron energy-loss spectroscopy (EELS) study was performed to determine the oxygen deficiency[25] while maintaining the electron-dose rate below the threshold for damage induced by the electron beam (Supplementary Figs. 11 and 12). The top STO layer showed a nearly identical shape of EELS edge to that from the STO bulk region in the same sample. This implies that the oxygen deficiency of the top STO is not severe enough to change the EELS fine structure. However, as even a small number of point defects (for which EELS is not sensitive enough) can significantly affect the band structure of oxide system, the absence of oxygen vacancies needs to be confirmed by an additional technique with a higher sensitivity.

To obtain more-detailed information about the oxygen-vacancy distribution, we performed depth-resolved cathodoluminescence spectroscopy (DR-CLS) analyses on the STO/LAO/STO hetero-structure. The DR-CLS, in which the penetration depth of the incident electron beam varies with beam energy, provides information on defect optical transitions as well as the band-to-band transition of the oxide material (Fig. 4a). The line profile of the oxygen-vacancy index, which directly reflects the density of oxygen vacancies, is given in Fig. 4b. The top STO exhibited a considerably smaller signature for oxygen vacancies, even smaller than that of the bulk STO substrate. The small amount of oxygen vacancies in the top STO showed no depth dependency, whereas the number of oxygen vacancies in the bulk STO increased with depth. The depth dependency of oxygen-vacancy distribution in the STO substrate is consistent with theoretical expectation[19]. As the formation energy of an oxygen vacancy is the highest at the n-type interface, the density of the oxygen vacancy is expected to increase with the distance away from the interface to the bulk region. Representative cathodoluminescence spectra obtained from the top STO and from the bulk STO substrate are given in Fig. 4c,d, respectively. The complete set of cathodoluminescence spectra is given in Supplementary Fig. 13. The spectra from the top STO are dominated by peaks related to the oxygen vacancy. Given the high sensitivity of the CLS technique, this result implies that the top STO does not contain any defects other than an extremely small number of oxygen vacancies, too small to be detected by EELS or X-ray measurements. All these structural studies unambiguously show that the 2DHG was realized in oxide heterostructures that contain minimal oxygen vacancies.

This study has directly demonstrated that the 2DHG formation is, in fact, achievable in high-quality oxide heterostructures. The next question is whether the interesting phenomena that have already been observed in 2DEG systems, such as a tunable spin–orbit interaction[26], superconductivity[4,5] and magnetism[3], can reveal new physics in the 2DHG system. In our structures, a high density of 2DEG coexists in proximity to the 2DHG layer. Although we utilized a comparatively thick LAO barrier for the separate electrical contacts, a much thinner barrier would make the two interfaces interact with each other more strongly. In such coupled quantum-well systems, indirect exciton states may be stabilized[27,28] or even new physical phenomena may occur because of the strong electron–hole coupling. The coexistence of 2DEG and 2DHG in a single oxide heterostructure enables an exploration of the exciting new physics of confined electron–hole systems, including long-lifetime bilayer excitons[27], Coulomb drag with spin–orbit coupling[29], bilayer electron–hole superconductivity and the Bose–Einstein condensation of excitons[30].

Methods

References

1. Ohtomo, A. & Hwang, H. Y. A high-mobility electron gas at the LaAlO₃/SrTiO₃ heterointerface. *Nature* **427**, 423–426 (2004).
2. Thiel, S., Hammerl, G., Schmehl, A., Schneider, C. W. & Mannhart, J. Tunable quasi-two-dimensional electron gases in oxide heterostructures. *Science* **313**, 1942–1945 (2006).
3. Brinkman, A. et al. Magnetic effects at the interface between non-magnetic oxides. *Nat. Mater.* **6**, 493–496 (2007).
4. Reyren, N. et al. Superconducting interfaces between insulating oxides. *Science* **317**, 1196–1199 (2007).
5. Caviglia, A. D. et al. Electric field control of the LaAlO₃/SrTiO₃ interface ground state. *Nature* **456**, 624–627 (2008).
6. Mannhart, J. & Schlom, D. G. Oxide interfaces—an opportunity for electronics. *Science* **327**, 1607–1611 (2010).
7. Cheng, G. L. et al. Sketched oxide single-electron transistor. *Nat. Nanotech.* **6**, 343–347 (2011).
8. Lesne, E. et al. Highly efficient and tunable spin-to-charge conversion through Rashba coupling at oxide interfaces. *Nat. Mater.* **15**, 1261–1266 (2016).
9. Mannhart, J., Blank, D. H. A., Hwang, H. Y., Millis, A. J. & Triscone, J. M. Two-dimensional electron gases at oxide interfaces. *MRS Bull.* **33**, 1027–1034 (2008).
10. Nakagawa, N., Hwang, H. Y. & Muller, D. A. Why some interfaces cannot be sharp. *Nat. Mater.* **5**, 204–209 (2006).
11. Huijben, M. et al. Electronically coupled complementary interfaces between perovskite band insulators. *Nat. Mater.* **5**, 556–560 (2006).
12. Herranz, G. et al. High mobility in LaAlO₃/SrTiO₃ heterostructures: origin, dimensionality, and perspectives. *Phys. Rev. Lett.* **98**, 216803 (2007).
13. Hwang, H. Y. et al. Emergent phenomena at oxide interfaces. *Nat. Mater.* **11**, 103–113 (2012).
14. Chen, Y. Z. et al. Extreme mobility enhancement of two-dimensional electron gases at oxide interfaces by charge-transfer-induced modulation doping. *Nat. Mater.* **14**, 801–806 (2015).
15. Pentcheva, R. & Pickett, W. E. Charge localization or itinerancy at LaAlO₃/SrTiO₃ interfaces: hole polarons, oxygen vacancies, and mobile electrons. *Phys. Rev. B* **74**, 035112 (2006).
16. Park, M. S., Rhim, S. H. & Freeman, A. J. Charge compensation and mixed valency in LaAlO₃/SrTiO₃ heterointerfaces studied by the FLAPW method. *Phys. Rev. B* **74**, 205416 (2006).
17. Pentcheva, R. et al. Parallel electron–hole bilayer conductivity from electronic interface reconstruction. *Phys. Rev. Lett.* **104**, 166804 (2010).
18. Huijben, M. et al. Local probing of coupled interfaces between two-dimensional electron and hole gases in oxide heterostructures by variable-temperature scanning tunneling spectroscopy. *Phys. Rev. B* **86**, 035140 (2012).
19. Zhong, Z. C., Xu, P. X. & Kelly, P. J. Polarity-induced oxygen vacancies at LaAlO₃/SrTiO₃ interfaces. *Phys. Rev. B* **82**, 165127 (2010).
20. Rubano, A. et al. Influence of atomic termination on the LaAlO₃/SrTiO₃ interfacial polar rearrangement. *Phys. Rev. B* **88**, 035405 (2013).
21. Cancellieri, C. et al. Polaronic metal state at the LaAlO₃/SrTiO₃ interface. *Nat. Commun.* **7**, 10386 (2016).
22. Luo, W. D., Duan, W. H., Louie, S. G. & Cohen, M. L. Structural and electronic properties of n-doped and p-doped SrTiO₃. *Phys. Rev. B* **70**, 214109 (2004).
23. Himmetoglu, B., Janotti, A., Peelaers, H., Alkauskas, A. & Van de Walle, C. G. First-principles study of the mobility of SrTiO₃. *Phys. Rev. B* **90**, 241204 (2014).
24. Koch, C. T. A flux-preserving non-linear inline holography reconstruction algorithm for partially coherent electrons. *Ultramicroscopy* **108**, 141–150 (2008).
25. Muller, D. A., Nakagawa, N., Ohtomo, A., Grazul, J. L. & Hwang, H. Y. Atomic-scale imaging of nanoengineered oxygen vacancy profiles in SrTiO₃. *Nature* **430**, 657–661 (2004).
26. Caviglia, A. D. et al. Tunable Rashba spin–orbit interaction at oxide interfaces. *Phys. Rev. Lett.* **104**, 126803 (2010).
27. Millis, A. J. & Schlom, D. G. Electron–hole liquids in transition-metal oxide heterostructures. *Phys. Rev. B* **82**, 073101 (2010).
28. Szymanska, M. H. & Littlewood, P. B. Excitonic binding in coupled quantum wells. *Phys. Rev. B* **67**, 193305 (2003).

29. Tse, W. K. & Das Sarma, S. Coulomb drag and spin drag in the presence of spin–orbit coupling. *Phys. Rev. B* **75**, 045333 (2007).

30. Eisenstein, J. P. & MacDonald, A. H. Bose–Einstein condensation of excitons in bilayer electron systems. *Nature* **432**, 691–694 (2004).

Author contributions

H.L. and C.B.E. conceived the project. C.B.E., M.S.R., E.Y.T., S.H.O. and L.J.B. supervised the experiments. H.L., J.W.L. and C.B.E. fabricated and characterized the thin-film samples. N.C. and M.S.R. carried out the electrical transport measurements. J.L., B.P., J.S. and S.H.O. carried out the STEM and in-line holography measurements. T.J.A. and B.N. performed the DR-CLS measurements. T.R.P. and E.Y.T. performed the theoretical calculations. H.Z. performed the synchrotron diffraction measurements. H.L., N.C., J.L., T.A., T.R.P., H.Z. and C.B.E. prepared the manuscript. C.B.E. directed the overall research.

Competing interests

The authors declare no competing financial interests.

Additional information

Supplementary information is available for this paper at https://doi.org/10.1038/s41563-017-0002-4.

Reprints and permissions information is available at www.nature.com/reprints.

Correspondence and requests for materials should be addressed to C.B.E.

Publisher's note: Springer Nature remains neutral with regard to jurisdictional claims in published maps and institutional affiliations.

Methods

Sample fabrication and electrical characterization. STO and LAO thin films were epitaxially grown on TiO_2-terminated $SrTiO_3$ (001) substrates using PLD with in situ RHEED monitoring[31,32]. To obtain the TiO_2-terminated substrates, as-received STO substrates were etched using buffered HF for 1 min and annealed at 900 °C for 6 h. The atomically flat surface of the thermally treated substrate is shown by atomic force microscopy images in Supplementary Fig.2b. During the film growth, the temperature of the PLD chamber was kept as 750 °C. The oxygen partial pressure for growing the LAO and STO films was 10^{-3} mbar and 10^{-2} mbar, respectively. After growing the STO/LAO films, the samples were in situ post-annealed under an oxygen ambient of 1 atm at 600 °C for 1 h. After the post-annealing process, the samples were slowly cooled down to room temperature in the oxygen ambient.

To make the square pattern of STO, photoresist masks were made on as-grown samples by a conventional photolithography technique. Then, the samples were slowly ion milled at a low power (milling rate of ~1 nm min^{-1}). After the ion milling, the samples were re-patterned by photolithography to fabricate the metal pads on them. The metal pads of Pt (~90 nm)/Al (~20 nm) were deposited by sputtering. Lastly, we used a commercial wire-bonding machine (WEST-BOND) to bond Al wires on top of the metal pads to contact to the top interface. The bottom interface was contacted by wire-bonding directly on top of the LAO surface. The electrical transport was measured through these contacts in Van der Pauw geometry.

The electrical transport measurements were conducted using an Oxford Maglab 2000 cryostat with a superconducting solenoidal magnet over a temperature range from 4 K to 300 K. Hall measurements were performed by sourcing positive and negative currents as the magnetic field was swept over a range from −2 to +2 T. The current polarity was switched at less than 1 Hz to avoid a.c. effects while maintaining an effectively constant field. The resistance was determined via a linear fit to the voltages measured at each current polarity. The areal carrier density was computed using the single-band equation $n_{sheet} = \left(\frac{dR_{xy}}{dB} q \right)^{-1}$ where R_{xy} is the Hall resistance, q is the electron charge and B is the applied magnetic induction. Both conducting interfaces were measured during the same field sweep, but neither was current sourced and nor was the voltage fixed in one interface during measurement of the other.

Theoretical calculations. The electronic structures of the LaO/TiO_2 (n-type) and AlO_2/SrO (p-type) interfaces were modelled using a supercell structure that contained two n- and p-type interfaces symmetrically arranged at the opposite sides of the central STO layer. This allowed us to eliminate an otherwise spurious electric field occurring in STO because of the periodic boundary condition. The overall supercell was 2(STO)/SrO/5(LAO)/TiO_2/6(STO)/5(LAO)/3(STO), where numerals represent the number of unit cells and it contains 220 atoms (Supplementary Fig. 1a shows half of the supercell). For the defect structures that contain oxygen vacancies, the in-plane size of the supercell was increased to $\sqrt{2} \times \sqrt{2}$ of the cubic perovskite unit-cell. The modelling was performed using density functional theory within the projected augmented wave method[33] for the electron–ion potential and the local density approximation (LDA) for exchange and correlation, as implemented in the Vienna ab initio simulation package (VASP)[34,35]. The calculations were carried out using a kinetic energy cutoff of 340 eV and an $8 \times 8 \times 1$ k-point mesh for Brillouin zone integration for a defect free structure and a $6 \times 6 \times 1$ k-point mesh for structures with oxygen vacancies. We fully relaxed the ionic coordinates with a force convergence limit of 0.01 eV per atom. The in-plane lattice constant was constrained to that of the LDA-calculated lattice constant of STO ($a = 0.386$ nm).

STEM–EELS and EDS measurements. For STEM measurements, the samples were prepared by following the standard lift-out technique using a focused ion beam (FIB) (JIB-4601F, Jeol). Sample thickness was around 100 nm after FIB milling and further reduced by Nanomill (Model 1040, Fischione) to the regime in which atomic-scale STEM imaging is possible. Surface damage induced by FIB was removed while varying the ion-beam energies in the range 500–900 eV in the Nanomill system. STEM–HAADF (HA, high-angle) images were obtained on a JEM-ARM200F microscope (Jeol) equipped with a spherical aberration corrector (ASCOR) operated at 200 kV. The probe convergence angle of approximately 22 mrad was used. The inner and outer angles of the HAADF detectors were 90 and 200 mrad, respectively. The electron-dose rate used for STEM–HAADF imaging was about 1.1×10^6 electrons nm^{-2} s^{-1}. The obtained STEM–HAADF images were deconvoluted with a simulated probe function (DeConv HAADF, HREM Research) to obtain good signal-to-noise data. EEL spectra and spectrum images were obtained at 200 kV using an EEL spectrometer (Gatan GIF Quantum ER) with an energy resolution of 0.8 eV. To evaluate how the electron probe introduces defects or modifies the charge balance, we determined the threshold electron-dose rate above which a detectable amount of damage is produced by monitoring the white-line intensity ratios and the fine structures of the EELS Ti–$L_{2,3}$ edge of STO and La–$M_{4,5}$ edge of LAO during the acquisition (Supplementary Fig. 11). The electron-dose rate used for STEM–EELS was 4.0×10^7 electrons nm^{-2} s^{-1}, which is below the measured threshold (5.7×10^7 electrons nm^{-2} s^{-1}).

The STEM–HAADF imaging mode combined with EDS (JED-EDS, Jeol) was used to obtain atomic-resolution elemental mapping data. A fast atomic-scale EDS mapping data of the sample was acquired within several minutes by utilizing a dual-type EDS detector (an effective X-ray detection area of a 100 mm² for each) with a large effective solid angle (~0.8 sr) and a highly focused electron probe (~1.1 Å) at the electron-dose rate of 7.7×10^6 electrons nm^{-2} s^{-1}. The resulting elemental maps were obtained by a multiple-frame summation up to less than 500 frames with 256×256 pixel resolution and the acquisition time of 10 μsec per pixel (maximum total acquisition time, ~5.5 min). The background noise floor in each map was removed by the Wiener filtering process.

Synchrotron CTR and COBRA. X-ray CTR measurements were carried out to quantify precisely the full atomic structures within each unit cell of the STO (ten unit cells)/LAO (40 unit cells) thin films epitaxially grown on a (001) STO substrate, including all the A-site and B-site cation and oxygen atomic positions. The CTR measurements were performed on a five-circle diffractometer with a χ-circle geometry using an X-ray energy of 20 keV (wavelength $\lambda = 0.6197$ Å) at sector 12-ID-D of the Advanced Photon Source, Argonne National Laboratory. The X-ray beam at the beamline has a total flux of 4.0×10^{12} photons s^{-1} and is vertically focused by beryllium compound refractive lenses down to a beam profile of ~20 μm. The 2D-diffraction images intersected at each step in the reciprocal space were acquired with a pixel 2D array area detector (Dectris PILATUS-1mm Si 100 K). To ensure a sufficient spatial resolution within each substrate-defined unit cell, we collected a large group of symmetry-inequivalent CTRs (for example, 12 specular and non-specular CTRs) with $L_{max} = 4.5$ reciprocal lattice units (r.l.u.) for a (001) pseudo-cubic system. The data-acquisition sampling density is 400 points per r.l.u., which is adequate to oversample each pronounced Laue fringe along each CTR. Overall, more than 15,000 structural factor amplitudes were collected during this measurement. The whole group of CTR data was subsequently analysed using the Fourier phase retrieval technique COBRA, which implements an iterative procedure of alternatively satisfying physical constraints in both real and reciprocal space to reconstruct the diffraction phases from measured diffraction intensities[36]. A complete 3D electron-density profile of the epitaxial thin film system was obtained from the fully retrieved overall complex structural factors. To determine the experimental errors, a general method, based on refining a parameterized model (for example, model-dependent nonlinear least-squares fitting), is not applicable to COBRA-derived electron-density profiles. Instead, we utilized a method called noise analysis to estimate the error bars of the parameters of interest. This method holds the same principle with the widely used bootstrap-resampling approach for uncertainty estimations in statistical analysis[37].

In-line electron holography measurement and analyses. In-line electron holography was carried out using a FE-TEM (Libra 200 MC, Carl Zeiss) operated at 200 kV equipped with a monochromator (CEOS) and in-column type OMEGA energy filter. An objective aperture of 10 μm in diameter was used to select the transmitted beam, which limits the spatial resolution to 0.6 nm. A total of 15 bright-field (BF) TEM images at defocus values ranging from −7 μm to +7 μm were acquired in 1 μm steps by exposing a 2,048 × 2,048 pixel fibre-optically coupled camera (UltraScan 1000 XP, Gatan) for 4 sec. All the images were recorded using the in-column energy filter to remove inelastically scattered electrons outside an energy window of 0 ± 5 eV. To minimize the electron-beam damage and secure a large field of view, the BF TEM images were obtained at a low magnification (×31,500) under an electron-dose rate of 9.7×10^3 electrons nm^{-2} s^{-1}. The obtained in-line electron holograms were used to reconstruct the phase shift of the transmitted beam using the full resolution wave reconstruction (FRWR) algorithm[38]. For an efficient sampling of high- and low-frequency information in the phase of the exit wavefunction, we used the FRWR algorithm with the phase-prediction function incorporated, which uses an approach similar to the transport intensity equation for the initial reconstruction of the high-frequency phase information (Supplementary Figs. 14 and 15). Then, the reconstructed phase data were converted into the map of the projected electrostatic potential by assuming the phase-object approximation for a non-magnetic material. The charge-density map was obtained from the potential data using Poisson's equation. In this process, the electric-field dependency of the dielectric constant was taken into account[39]. However, the charge-density values might be overestimated because of the inaccuracy in determining the thin-film dielectric constants.

DR-CLS measurement and analyses. DR-CLS[40,41] was performed using a Physical Electronics Inc. (PHI) 110-10 glancing incidence election gun operated with beam voltages from 0.5 kV to 4.5 kV and an emission current controlled to provide a constant power of 1 mW with varying voltages under ultrahigh vacuum (UHV) conditions. The emitted photons were collected by a CaF_2 lens in vacuum, and passed through a sapphire window port of the UHV chamber into an Oriel F-number matcher. The collected light was then dispersed through an Oriel MS260i monochromator using a grating with a 300 nm blaze into an Andor iDus open-electrode charge-coupled detector. The sample was coated with a gold overlayer 10 nm in thickness and a grounded copper grid above it to minimize charging from the incident electron beam[42]. The oxygen-vacancy index shown

in Fig. 4b is defined as the intensity ratio between the CLS peak at 2.9 eV and the peak at 3.6 eV. The CLS peaks at 2.9 eV and at 3.6 eV represent the oxygen-vacancy-related transition and the bandgap transition of STO, respectively[43].

Data availability. The data that support the findings of this study are available from the corresponding author on reasonable request.

References

31. Bark, C. W. et al. Tailoring a two-dimensional electron gas at the LaAlO₃/SrTiO₃ (001) interface by epitaxial strain. *Proc. Natl Acad. Sci. USA* **108**, 4720–4724 (2011).
32. Bi, F. et al. Room-temperature electronically-controlled ferromagnetism at the LaAlO₃/SrTiO₃ interface. *Nat. Commun.* **5**, 5019 (2014).
33. Blochl, P. E. Projector augmented-wave method. *Phys. Rev. B* **50**, 17953–17979 (1994).
34. Kresse, G. & Furthmuller, J. Efficient iterative schemes for ab initio total-energy calculations using a plane-wave basis set. *Phys. Rev. B* **54**, 11169–11186 (1996).
35. Kresse, G. & Joubert, D. From ultrasoft pseudopotentials to the projector augmented-wave method. *Phys. Rev. B* **59**, 1758–1775 (1999).
36. Zhou, H. et al. Anomalous expansion of the copper–apical-oxygen distance in superconducting cuprate bilayers. *Proc. Natl Acad. Sci. USA* **107**, 8103–8107 (2010).
37. Zhou, H., Pindak, R., Clarke, R., Steinberg, D. M. & Yacoby, Y. The limits of ultrahigh-resolution X-ray mapping: estimating uncertainties in thin-film and interface structures determined by phase retrieval methods. *J. Phys. D.* **45**, 195302 (2012).
38. Koch, C. T. Towards full-resolution inline electron holography. *Micron* **63**, 69–75 (2014).
39. Janolin, P. E. Strain on ferroelectric thin films. *J. Mater. Sci.* **44**, 5025–5048 (2009).
40. Zhang, J. et al. Depth-resolved subsurface defects in chemically etched SrTiO₃. *Appl. Phys. Lett.* **94**, 092904 (2009).
41. Brillson, L. J. Applications of depth-resolved cathodoluminescence spectroscopy. *J. Phys. D.* **45**, 183001 (2012).
42. Asel, T. J. et al. Near-nanoscale-resolved energy band structure of LaNiO₃/La₂/₃Sr₁/₃MnO₃/SrTiO₃ heterostructures and their interfaces. *J. Vac. Sci. Technol. B* **33**, 04E103 (2015).
43. Rutkowski, M. M., McNicholas, K., Zeng, Z. Q., Tuomisto, F. & Brillson, L. J. Optical identification of oxygen vacancy formation at SrTiO₃–(Ba,Sr)TiO₃ heterostructures. *J. Phys. D.* **47**, 255303 (2014).